

Emerging technologies and advanced analyses for non-invasive near-surface site characterization

*Original*

Emerging technologies and advanced analyses for non-invasive near-surface site characterization / Abbas, A., Aimar, M., Yust, M., Cox, B., Foti, S.. - In: SOILS & ROCKS. - ISSN 1980-9743. - ELETTRONICO. - 47:3(2024), pp. 1-18. [10.28927/sr.2024.006923]

*Availability:*

This version is available at: 11583/2987085 since: 2024-03-18T18:02:32Z

*Publisher:*

Brazilian Association for Soil Mechanics and Geotechnical Engineering (ABMS)

*Published*

DOI:10.28927/sr.2024.006923

*Terms of use:*

This article is made available under terms and conditions as specified in the corresponding bibliographic description in the repository

*Publisher copyright*

(Article begins on next page)

# Emerging technologies and advanced analyses for non-invasive near-surface site characterization

Aser Abbas<sup>1#</sup> , Mauro Aimar<sup>2</sup> , Michael Yust<sup>3</sup> , Brady R. Cox<sup>1</sup> , Sebastiano Foti<sup>2</sup>  **Review Article**

## Keywords

Shear wave velocity  
Rayleigh waves  
DAS  
Damping  
FWI  
Machine learning

## Abstract

The in-situ small-strain shear modulus of soil and rock materials is a parameter of paramount importance in geotechnical modeling. It can be derived from non-invasive geophysical surveys, which provide the possibility of testing the subsurface in its natural and undisturbed condition by inferring the velocity of propagation of shear waves. In addition, for soil dynamics and earthquake engineering applications, the small-strain damping ratio plays a relevant role, yet its estimation is still challenging, lacking consolidated approaches for its in-situ evaluation. Recent advancements in instrumentation, such as distributed acoustic sensing (DAS), combined with advanced analysis methodologies for the interpretation of seismic wave propagation (e.g., machine learning and full waveform inversion), open new frontiers in site characterization. This paper presents and compares some advanced applications of measuring 1D and 2D variations in shear wave velocity and attenuation in-situ with reference to a specific case history.

## 1. Introduction

Non-invasive subsurface imaging techniques utilizing seismic wave propagation have garnered escalating attention in recent decades owing to their remarkable cost-effectiveness compared to conventional invasive site characterization methods and their potential to cover large areas. These imaging techniques primarily focus on capturing two crucial soil parameters of particular interest in geotechnical engineering: the small-strain shear wave velocity ( $V_s$ ) and the small-strain damping ratio in shear ( $D_s$ ).  $V_s$  is directly related to the small-strain shear modulus ( $G_0$  or  $G_{max}$ ), representing the stiffness of the soil, while  $D_s$  quantifies the soil internal energy dissipation at low strains. This paper provides a review of some of the latest advancements in noninvasive subsurface imaging techniques for the estimation of  $V_s$  and  $D_s$  and their practical application at a well-characterized case history site called the Hornsby Bend site in Austin, Texas, USA. The subsequent paragraphs highlight the importance of  $V_s$  and  $D_s$  in geotechnical engineering applications and discuss the challenges and advancements in the noninvasive techniques developed for their estimation.

$V_s$  and  $D_s$  play a key role in evaluating the response of soil deposits to both general dynamic loading and ground

motion amplification caused by earthquakes. In regard to seismic loads,  $V_s$  and  $D_s$  are especially important parameters to quantify when the soil is subjected to low-intensity shaking (e.g., Tao & Rathje, 2019; Rodriguez-Marek et al., 2021; Fernandes et al., 2023). For instance, Rodriguez-Marek et al. (2021) observed that  $D_s$  is the most influential parameter at high frequencies, with an impact even more relevant than  $V_s$ , whereas the low-frequency soil response is mainly affected by  $V_s$  of shallow layers. According to Foti et al. (2021),  $D_s$  has a substantial influence on the seismic amplification in deformable soil deposits. However, this influence is less pronounced under conditions of strong shaking that strain the soil sufficiently to induce nonlinear soil behavior. Additionally, in a site-specific study, Foti et al. (2021) compared the amplification resulting from the epistemic uncertainty in  $D_s$  with that caused by  $V_s$  and the nonlinear soil behavior modeled using modulus reduction and damping (MRD) curves. They found that a change in  $D_s$  leads to a significant variation in amplification compared to the overall variability of the results. This effect is particularly relevant at high frequencies and near the resonance peak, even under higher seismicity conditions.

Furthermore, studies such as Kouroussis et al. (2011), Papadopoulos et al. (2019), and Santos et al. (2016) highlight the importance of  $V_s$  and  $D_s$  in assessing vibrational impact.

#Corresponding author. E-mail address: aser.abbas@usu.edu

<sup>1</sup>Utah State University, Department of Civil and Environmental Engineering, Logan, UT, USA.

<sup>2</sup>Politecnico di Torino, Dipartimento di Ingegneria Strutturale, Edile e Geotecnica, Torino, Italia.

<sup>3</sup>Slate Geotechnical Consultants, Oakland, CA, USA.

Submitted on July 1, 2023; Final Acceptance on December 20, 2023; Discussion open until November 30, 2024.

<https://doi.org/10.28927/SR.2024.006923>



This is an Open Access article distributed under the terms of the Creative Commons Attribution License, which permits unrestricted use, distribution, and reproduction in any medium, provided the original work is properly cited.

The small-strain and anelastic properties of the soil significantly influence the energy transmission from the source, its propagation, and the resulting motion at the receiver. These properties directly impact the amplitude and frequency content of the vibrations. For instance, Lombaert & Degrande (2003) and Lombaert et al. (2006) observed that when dealing with rail traffic as the noise source, uncertainties in defining the spatial variation of dynamic soil characteristics lead to poor agreement between simulated and experimental data. Rail vehicles mainly generate high-frequency signals, reaching up to 200 Hz (Pyl, 2004). Due to their short wavelengths, these signals are highly sensitive to local heterogeneities in the soil deposit. Moreover, Schevenels (2007) demonstrated the impact of uncertainties in  $D_s$  and  $V_s$  on free-field wave propagation, whose variability exponentially increases with the frequency, especially at large distances from the source.

The small-strain dynamic soil properties also play an important role in soil-structure interaction problems, where the deformability of the supporting soil impacts both the fundamental period and the energy dissipation of the system (Veletsos & Meek, 1974). Among these properties,  $V_s$  holds particular significance as it directly governs soil deformability, which is a key factor in this phenomenon (Veletsos & Meek, 1974). Energy dissipation, on the other hand, arises from various sources, including inelastic phenomena within the structure, hysteretic dissipation in the soil deposit, and radiation damping. Radiation damping refers to the geometric effect of waves radiating from the foundation-soil interface, carrying energy away from the foundation system as they propagate outward. It is commonly assumed that radiation damping represents the primary mechanism for energy dissipation, especially at small strains. However, Martakis et al. (2017) observed through centrifuge tests that significant dissipation also occurs due to hysteretic effects linked to the intrinsic dissipation of the soil, even at small strains.

The preceding paragraphs underscore the importance of accurately estimating  $V_s$  and  $D_s$  for dynamic modeling of seismic and general vibration problems. Traditionally, these small-strain soil properties have been estimated through laboratory testing or empirical relationships (e.g., Darendeli, 2001; Menq, 2003; Ciancimino et al., 2020). However, their in-situ estimated values often deviate from those obtained in the laboratory. This deviation can be attributed to the disturbances that inevitably occur during the acquisition of soil samples for laboratory testing, leading mostly to a reduction in soil stiffness (e.g., Stokoe & Santamarina, 2000). Additionally, at the site scale, complex wave propagation phenomena (e.g., wave scattering) result in additional energy dissipation beyond material dissipation, which cannot be captured accurately through laboratory tests (e.g., Stewart et al., 2014; Tao & Rathje, 2019). Geophysical field measurements offer the advantage of estimating the ground response in its natural state thus mitigating the uncertainties associated with sample disturbance and scale effects often encountered when working with rock-like materials. Overall, non-invasive

techniques investigate a large volume of the medium, whose size depends on the array geometry (Comina et al., 2011; Passeri, 2019), providing parameter estimates at a scale compatible with those of geotechnical systems. Furthermore, some design criteria in geoen지니어ing directly rely on these testing procedures. For instance, rail infrastructure design requires the train speed to be smaller than a “critical” speed, corresponding to the Rayleigh phase velocity,  $V_R$ , of the underlying medium (e.g., Connolly et al., 2015). Indeed, at higher speeds, the amplitude of track vertical deflection dramatically increases (Timoshenko, 1927; Krylov, 1995; Madshus & Kaynia, 2000; Madshus et al., 2004). For this reason, the rail operational speed is often determined through a dispersion diagram, which involves the experimental  $V_R$  at various frequencies as an input parameter, determined through surface wave-based geophysical techniques (Thompson, 2009). Finally, the field-based small-strain estimates of  $V_s$  and  $D_s$  can be used in conjunction with laboratory tests to map and un-normalize the nonlinear mechanical response of soil, which is most easily characterized in the lab at strains ranging from moderate to large. This approach enables the development of advanced numerical models or simplified procedures for evaluating the behavior of geotechnical systems subjected to either static or dynamic loading (e.g., settlement of shallow foundations and seismic site response) across a broad range of induced strains.

Given the importance of accurately estimating  $V_s$  and  $D_s$  in situ, the field of geophysical imaging based on seismic wave propagation is continuously advancing, introducing new innovations aimed at increasing imaging resolution and reducing uncertainty. These innovations encompass improvements in both data acquisition systems (DAQ) and imaging methodologies. A notable recent development in data acquisition is the utilization of distributed acoustic sensing (DAS) for seismic wave measurements. DAS offers unprecedented spatial resolutions (on the order of meters) and length scales (on the order of tens of kilometers), surpassing conventional sensing technologies (Soga & Luo, 2018). Further details on DAS technology, which is employed as the DAQ for most of the 1D and 2D imaging techniques discussed in this paper, are provided in a separate, dedicated section later in this paper. This paper also highlights some of the significant advancements in imaging techniques, encompassing both 1D and 2D approaches. In the field of 1D imaging, two notable developments have emerged. Firstly, the utilization of DAS as the DAQ for 1D multichannel analysis of surface waves (MASW). Secondly, the joint estimation of phase velocity and phase attenuation data within a 1D MASW test setup, achievable using either geophones or DAS as the DAQ. This paper demonstrates the pioneering use of DAS for jointly characterizing the stiffness and dissipative parameters of a soil deposit. In the realm of 2D imaging, the presented techniques comprise the application of 2D MASW using DAS data, the utilization of machine learning for 2D imaging, and the use of full waveform inversion (FWI) with DAS data.

All of these 1D and 2D imaging techniques were successfully applied at a well-characterized case history site called the Hornsby Bend test site, providing a valuable opportunity to compare and discuss their results.

The subsequent sections of the paper are organized as follows. First, a brief overview of DAS technology is presented, highlighting its key features and capabilities. Following that, the testing conducted at the Hornsby Bend site is discussed. The paper then delves into the advancements in 1D and 2D imaging techniques in regard to measuring  $V_s$  and  $D_s$  at the Hornsby Bend site. Then, a discussion about the advantages and disadvantages of each technique is presented. Lastly, a comprehensive subsurface imaging experiment conducted at the Newberry site in Florida, USA utilizing some of the latest sensing technologies is showcased.

## 2. The DAS technology

DAS is an innovative technique that transforms fiber-optic cables into a distributed array of ground motion sensors (Cox et al., 2012; Yu et al., 2019). This rapidly evolving technology allows for the simultaneous collection of high-resolution data with small channel separations (e.g., 1-m) over long arrays spanning kilometers, making it highly suitable for near-surface imaging applications. Unlike traditional geophones that measure particle velocity ( $\partial u/\partial t$ ) at discrete points along the acquisition array (Figure 1a), DAS records the spatially-averaged axial strain  $e(r,t)$  induced on the fiber-optic cable by the passing wavefield. Here, “ $r$ ” represents the location coordinate and “ $t$ ” represents the time instant. When properly coupled with the ground, the passage of mechanical waves generates an axial strain in the fiber-optic cable that coincides with the horizontal, in-line strain  $\epsilon(r,t)$  in the ground. An interrogator unit (IU) reads the consequent shift in phase lag of a laser pulse traveling in the cable, induced by the variation in the length of the cable.

Thus DAS measurements represent the variation in phase difference over a reference length  $2g$ , called gauge length, around the investigated location, from which the average strain  $e(r,t)$  is derived (Figure 1b; Grattan & Sun, 2000). The resulting average strain at each measurement point can be linked with the displacement  $u(r,t)$ , as it equals the difference of the radial displacement at two points separated by a distance equal to the gauge length (Mateeva et al., 2014; Bakku, 2015; Jousset et al., 2018; Vantassel et al., 2022b):

$$e(r,t) = \frac{1}{2g} [u(r+g,t) - u(r-g,t)] \quad (1)$$

It is noteworthy that the gauge length is not necessarily linked with the channel separation (i.e., the distance between two subsequent measurement points). The gauge length plays a crucial role in the spatial sampling quality, as it limits the range of investigable wavelengths. In the simple scenario of a spatially harmonic radial displacement field, it is demonstrated that the averaging procedure (i.e., the mapping from  $\epsilon(r,t)$  to  $e(r,t)$ ) is equivalent to applying a lowpass filter (such as a sinc filter) in the wavenumber domain (e.g., Bakku, 2015). This filtering tends to attenuate wave components with shorter wavelengths  $\lambda$ , particularly affecting the high-frequency components of the Rayleigh wavefield (Figure 1c). Increasing the gauge length results in a greater loss of information for short-wavelength data, although it improves the overall signal quality and signal-to-noise ratio (e.g., Bakulin et al., 2020). Therefore, selecting an optimal gauge length is a critical task that should consider various factors such as the acquisition setup, source quality, magnitude of incoherent noise, and the desired range of investigated wavelengths. A possible strategy to overcome the resolution issues induced by spatial averaging is to conduct multiple measurements where the gauge length is modified at each

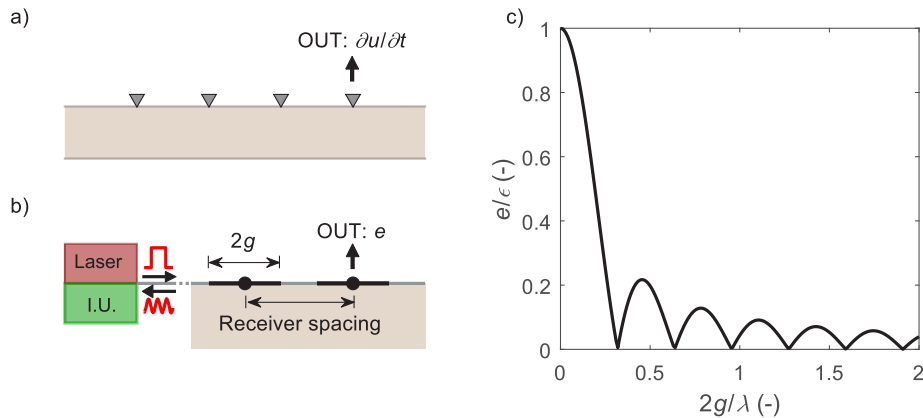


**Figure 1.** a) Schematic model of an acquisition system based on geophones, wherein the output (labeled as “OUT”) is the particle velocity  $\partial u/\partial t$ ; b) Schematic model of the DAS system, where a source generates a laser pulse which is then interpreted by an interrogator unit (labeled as I.U.) and the output (labeled as “OUT”) is the average strain  $e$  [modified from Bakku (2015)]; c) Amplitude response in terms of  $e/\epsilon$  ratio, as a function of the wavelength-normalized gauge length  $2g/\lambda$ .

step (Bakku, 2015). It is worth noting that interpreting DAS-recorded data, which provides a spatially averaged measure of the strain field, is slightly more complex compared to conventional acquisition devices. Nonetheless, DAS is increasingly being used for invasive geophysical tests (e.g., Mateeva et al., 2014; Kuvshinov, 2016), ambient noise vibrations (e.g., Hornman et al., 2013; Freifeld et al., 2016; Yavuz et al., 2016; Ajo-Franklin et al., 2017) and MASW testing (Galan-Comas, 2015; Lancelle, 2016; Costley et al., 2018; Song et al., 2018; Vantassel et al., 2022b).

### 3. Innovative processing techniques and DAS

#### 3.1 Reference dataset: Hornsby Bend

The Hornsby Bend site (HB, 30°13.918'N, 97°38.631'W – in the WGS84 Datum) is located on the outskirts of Austin, Texas, USA. This site has been the subject of extensive invasive and noninvasive site characterization studies in recent years. The noninvasive testing conducted at the site and utilized in this paper involved the deployment of two parallel 200 meter-long fiber-optic cables (refer to Figure 2a), one manufactured by NanZee and the other by AFL. These cables were interconnected at the far end of the array by splicing the NanZee and AFL cables together, enabling simultaneous recording on both cables. On the near-side of the array, the NanZee cable was connected to an OptaSense ODH4 IU, while the AFL fiber was properly terminated to minimize end-reflections. The ODH4 IU was configured with the gauge length

and channel separation set to 2.04 m and 1.02 m, respectively. These values represent the shortest gauge length and channel separation allowed by the ODH4. Consequently, the DAS recorded waveforms represent an average response over the 2.04 m gauge length surrounding each channel location (i.e., every 1.02 m). The IU sampling frequency, or ping rate, was set at 100 kHz. After acquiring the data, the raw measurements underwent down sampling to 1 kHz and high-pass filtering above 3 Hz to remove low-frequency artifacts linked with laser drift and static strains.

Two geophone arrays were also deployed in conjunction with the fiber-optic cables: a vertical geophone array and a horizontal geophone array oriented in line with the DAS fiber optic cables. Each array comprised 48 geophones, uniformly spaced at 2 m intervals, resulting in a total array length of 94 m as shown in Figure 2a. To capture the geophone signals, four interconnected 24-channel Geometrics Geode seismographs were utilized, enabling simultaneous recording from both the vertical and horizontal geophone arrays. All signals were acquired using a sampling rate of 1 kHz. The geophone array and DAS fiber-optic cables were employed to simultaneously record actively-generated surface waves from various sources. These sources encompassed highly-controlled vibroseis shaker trucks and more variable impact sources. The vibroseis sources comprised the three-dimensional shaker, T-Rex, and the highly-mobile one-dimensional shaker, Thumper, both from the Natural Hazards Engineering Research Infrastructure at the University of Texas at Austin (NHERI@UTexas) experimental facility (Stokoe II et al., 2020). Additionally, an

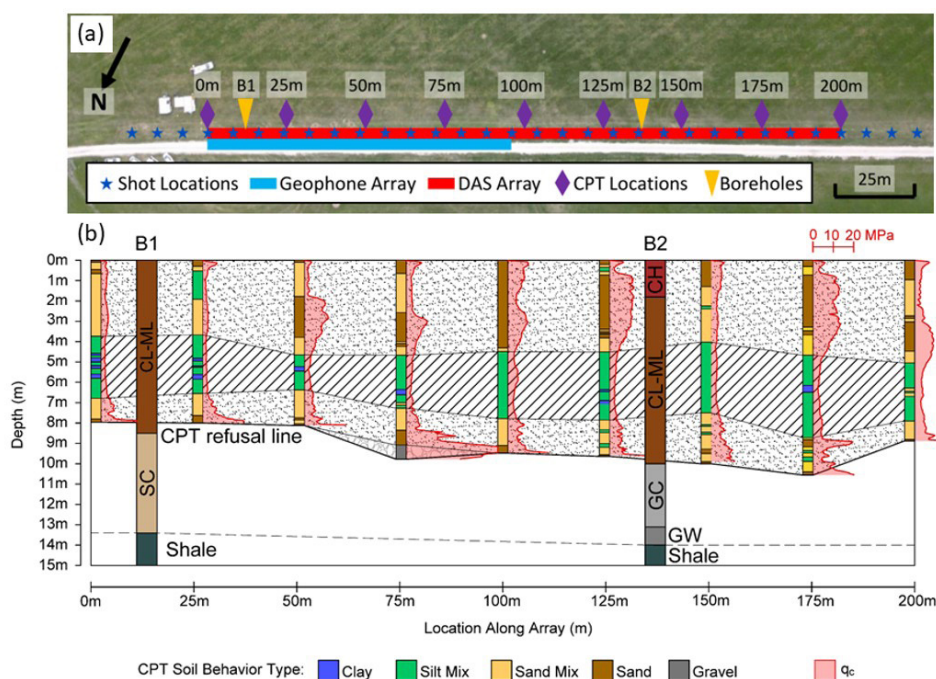


**Figure 2.** a) Aerial view of the Hornsby Bend test site showing the locations of CPT tests and boreholes as well as the DAS fiber optic cable, the geophone array, and the vibroseis shot locations; b) Geological cross section.

instrumented 5.4 kg sledgehammer from PCB Piezotronics was used as an impact source. T-Rex was utilized for shaking in all three directions: vertically, horizontally in-line, and horizontally cross-line. It generated a 12-second chirp signal with frequencies linearly swept from 3 to 80 Hz, providing a maximum force output of approximately 270 kN in the vertical direction and 130 kN in the horizontal directions. Thumper was used to produce a 12-second chirp signal in the vertical direction with frequencies linearly swept from 5 to 200 Hz, offering a maximum force output of approximately 27 kN in the vertical direction. For the vibroseis sources, three sweeps were conducted at each source location, whereas five impacts were performed using the sledgehammer. These sources were used at various locations around the site, however, for the purposes of this paper, only the source locations along the linear array alignment will be discussed. A significant portion of the noninvasive dataset from testing conducted at the Hornsby Bend site is accessible to the public through DesignSafe-CI (Vantassel et al., 2022a).

In addition to the noninvasive testing, nine cone penetration tests (CPT) soundings were carried out at 25 m intervals along the fiber-optic cable, covering the range from 0 to 200 m, as indicated in Figure 2a. These CPT soundings were performed on three different dates, spaced out over a span of approximately eight months. Yust et al. (2022) utilized the soil behavior type index value (Ic) method developed by Robertson (2009) to analyze the collected CPT data. Based on their analysis, they developed the subsurface cross section shown in Figure 2b down to the depths of CPT refusal. According to Yust et al. (2022), the site comprises three distinct layers above the depth of CPT refusal. These layers include a shallow granular layer (between depths of approximately 0 to 4 m) consisting of sand and sand mix, an intermediate cohesive layer (between depths of approximately 4 to 7 m) comprising clay and silt, and a deeper granular layer (between depths of approximately 7 to 10 m) composed of sand and sand mix. The depth of CPT refusal along the cable varied between 7.96 and 10.56 m, with an average depth of 9.15 m. In this study, the original cross-section developed by Yust et al. (2022) has been

further extended from its original depth of approximately ten meters down to 15 m, as shown in Figure 3b. This extension enables the depiction of the shale layer depth, which was determined using data acquired from two recently drilled boreholes at the Hornsby Bend site. Both the first borehole (B1) positioned 12.5 m from the starting point of the geophone array, and the second borehole (B2), located 137.5 m away (refer to Figure 2b), confirmed the existence of a shale layer at an approximate depth of 13.5 m beneath the ground surface. Furthermore, seismic downhole (DH) testing was conducted in borehole B1, reaching a depth of 24 m with a receiver interval of 1 m, which led to the identification of four distinct velocity layers in the subsurface (discussed later in the paper).

### 3.1.1 1D MASW processing for the joint estimation of S-wave velocity and damping ratio

A promising technique for obtaining in-situ estimates of  $V_s$  and  $D_s$  relies on MASW (Nolet & Panza, 1976; McMechan & Yedlin, 1981; Gabriels et al., 1987; Park et al., 1999; Foti, 2000). This technique relies on the measurement of propagation characteristics of surface waves (typically, Rayleigh waves) and the testing procedure can be divided into three main steps:

- Data acquisition: a waveform generated by an artificial source is recorded along a linear array of sensors (typically, geophones) on the ground surface.
- Data processing: based on variations of phase lag and amplitude of surface waves along the array, the corresponding propagation speed (i.e., the phase velocity  $V_R$ ) and spatial attenuation of the amplitude (i.e., the phase attenuation  $\alpha_R$ ) are derived, as a function of the frequency. The frequency-dependence of  $V_R$  and  $\alpha_R$  is a combined effect of geometric dispersion, which results from the variation of mechanical properties with depth, and intrinsic dispersion, due to the constitutive behavior of linear viscoelastic media.
- Inversion: the  $V_s$  and the  $D_s$  profile with depth are obtained through an inversion scheme, where a

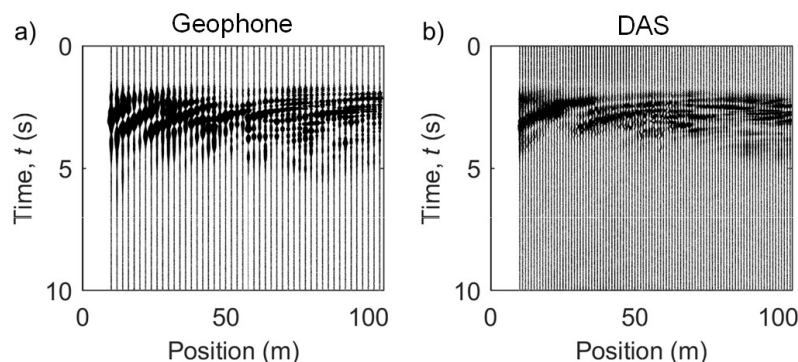


**Figure 3.** Recorded data at the Hornsby Bend site: a) Time histories of particle velocity recorded by the geophone array; b) Time histories of average radial strain recorded by DAS. Data refer to the wavefield generated from the active source located at an offset equal to 10 m.

theoretical soil model is calibrated to match the experimental  $V_R$  and  $\alpha_R$ .

In MASW testing, the main advantage of the DAS technology with respect to conventional acquisition devices is the enhanced spatial resolution using low-cost instrumentation. Indeed, DAS allows for dense spatial sampling of the wavefield, potentially along a broad array extent. Conversely, achieving the same spatial resolution with ordinary receiver arrays would require a large number of sensors, entailing severe economic and logistic issues. Furthermore, high quality measurements can be even obtained from conventional fiber-optic cables, that are not specifically designed for seismic investigation and already deployed in the ground (e.g., the telecommunication infrastructure; Jousset et al., 2018). Therefore, the per-channel cost is moderately low. Applications of this technology to MASW surveys demonstrated that the dispersion estimates well match those obtained from geophone measurements (Galan-Comas, 2015; Vantassel et al., 2022b). Furthermore, the DAS acquisition tends to better identify higher propagation modes (Galan-Comas, 2015). However, fiber-optic systems are uniaxial devices, recording only perturbations acting in the longitudinal direction, and the correct location of measurement points may be uncertain in some cases (e.g., in the case of fiber overstuffing; Bakku, 2015). Also, the signal-to-noise ratio of measured data is lower compared to geophones. The lower quality in recorded traces limits the repeatability of the survey (Costley et al., 2018) and the reliability of the estimated wave parameters in the presence of weak signals (Mestayer et al., 2012). Finally, as explained above, the measurement technique involved in this technology partially limits the minimum investigable wavelengths at greater values than the one defined by the Nyquist-Shannon theorem (Lancelle, 2016; Bakulin et al., 2020). Therefore, the characterization of high-frequency R-wave data might be challenging.

Different acquisition layouts were investigated at the Hornsby Bend site to assess the influence of the DAQ type on the estimated dispersion and attenuation data, through the canonical 1D processing procedure. The first 94 m section of the fiber-optic cable, which is adjacent to the geophone array, is selected in this study to ensure a consistent comparison between results, as they sample a comparable volume of the soil deposit. This study refers to waveforms generated at shot points located at 5 m, 10 m, 20 m, and 40 m offset from the closest measurement point (i.e., 0 m; refer to Figure 3a). Additionally, it only utilizes waveforms created by the Thumper truck, which generated a 12-s long chirp signal, with frequency shifting from 5 Hz to 200 Hz. As an example, Figure 3a-3b reports the time histories of recorded data in the Hornsby Bend site using the geophone and the DAS arrays, with the active source located at an offset equal to 10 m.

As noted above, Vantassel et al. (2022b) showed that it is possible to extract equivalent surface wave dispersion data from seismic measurements made using a traditional geophone array and DAS. Moreover, they demonstrated that frequency-dependent normalization of the dispersion image

removes the effect of scaling, integration, and differentiation on the acquired waveforms, thereby mitigating the need to convert the measurements into consistent engineering units prior to comparing dispersion data. Thus, Vantassel et al. (2022b) rigorously demonstrated the potential for extracting high-resolution, multi-mode surface wave dispersion data using DAS measurements and MASW-type processing.

Aimar et al. (2023) showcased the potential of exploiting DAS data for the joint estimation of the phase velocity and phase attenuation data. These quantities were obtained from the vertical geophone waveforms through application of the recently developed Cylindrical Frequency-Domain BeamForming – Attenuation algorithm with Modal Filtering (CFDBFaMF; Aimar et al. (2024a)). The extraction of the R-wave parameters from DAS data adopts a modified version of the CFDBFaMF, which implements an average strain-based beamforming [further details are available in Aimar et al. (2024a)]. In this way, the procedure properly models the spatial variation of the amplitude and phase of the average radial strain. Figure 4 compares the estimated modal dispersion and attenuation data for the first two propagation modes (labeled as R0 and R1, respectively), obtained from the interpretation of the DAS and the geophone array data. In this case, the data distribution is represented by the interval around the median value, the width of which equals one logarithmic standard deviation. Data statistics are obtained by combining results from different source offsets, in consistency with the multi-offset approach (Cox & Wood, 2011).

In general, dispersion and attenuation data well match with each other, particularly for the R0 mode. For the R1 mode, the DAS data does not allow phase velocity and attenuation estimates to be made over as broad a frequency range, being more limited at lower frequencies. This partially limits the capability of the DAS system in characterizing deeper layers. However, the corresponding degree of variability in the phase velocity and attenuation data derived from DAS is generally less than or equal to the variability affecting the geophone-based parameters. This result is quite surprising, as the signal-to-noise ratio of DAS records has been reported in other studies to be slightly lower than geophone records, hence, higher variability in the DAS-derived attenuation was expected. A possible reason behind the low data scatter can be the remarkably larger number of measurement points that the DAS system includes, that provides a more exhaustive dataset of wavefield values to better constrain the velocity and the attenuation estimates.

Finally, experimental Rayleigh-wave data were mapped into profiles of  $V_s$  and  $D_s$  versus depth, by means of the inversion procedure developed by Aimar et al. (2024b). This operation was carried out through an improved Monte Carlo scheme, which implements a smart sampling technique of the model parameter space, by exploiting the scaling properties of the Rayleigh wave parameters in linear viscoelastic media. These properties allow a significant saving in computation time, preserving the quality of the resulting ground models at the same time. For simplicity,

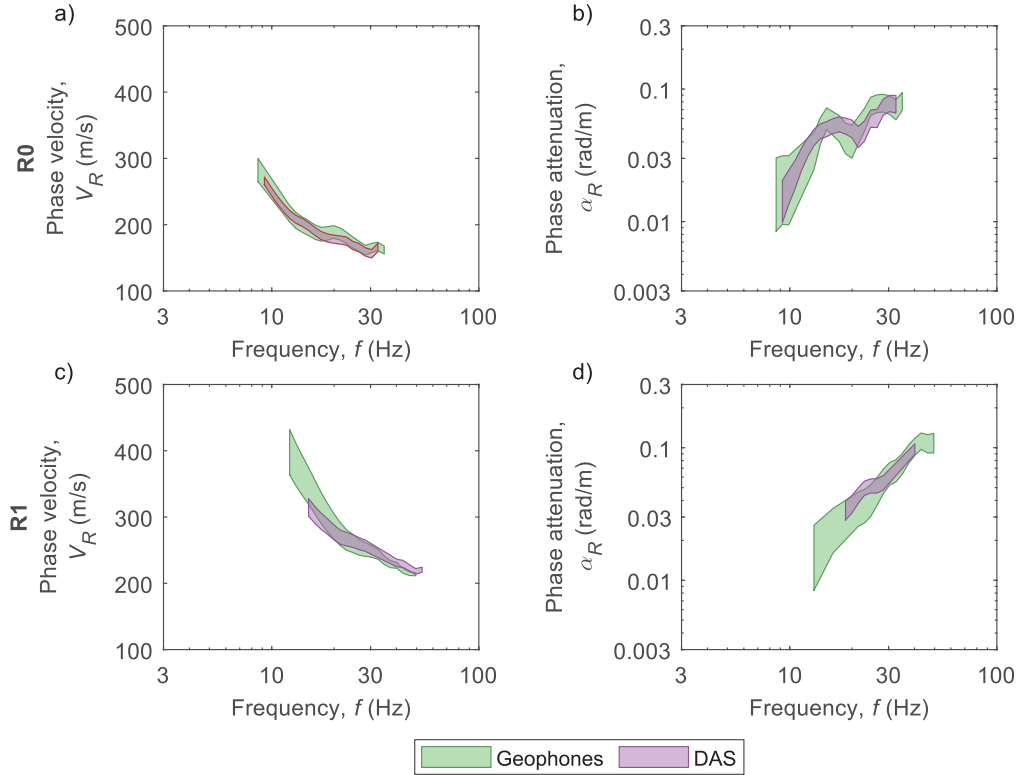


**Figure 4.** Comparison between the estimated dispersion and attenuation curves from the DAS and the geophone data at the Hornsby Bend site: a-b) Resulting dispersion (a) and attenuation (b) curves for the fundamental mode, R0; c-d) Resulting dispersion (c) and attenuation (d) curves for the first higher mode, R1. Estimated data are represented in terms of intervals given by one logarithmic standard deviation around the median value; after Aimar et al. (2023).

the model identification adopts a three-layer ground model, consistently with the stratigraphy inferred by cone penetration soundings carried out close to the DAS array (refer to Figure 2b). For each layer, an adequate range of layer thicknesses, S-wave velocities and damping ratios were investigated, whereas the mass density and Poisson's ratios were fixed at realistic values. The inversion was run using 10,000 trial earth models. Forward dispersion and attenuation modeling was carried out through the EDT toolbox (Schevenels et al., 2009). Model selection was based on a proper misfit function, wherein fitting errors between theoretical curves and experimental data were weighted as a function of the uncertainties affecting  $V_R(\omega)$  and  $\alpha_R(\omega)$ .

Figure 5 shows results for the best fitting 30 models. Inverted S-wave velocity and damping ratio profiles are relatively well constrained, and the velocity and dissipation structures are clearly identifiable in the near-surface layers. Specifically, the resulting  $V_S$  model exhibits a gradual increase in stiffness with depth. The depths of the identified layers interfaces are about 4 m and 12-13 m. This result is consistent with the main geological interfaces inferred at the site and with information from past geophysical surveys. The estimated  $D_S$  profiles are affected by greater variability, which increases with depth. Specifically,  $D_S$  is about 5% in the near-surface layer, and increases to around 8% in the layer

below. As for the half-space, the variability in both  $V_S$  and  $D_S$  dramatically increases with respect to shallow layers. Indeed, the few amounts of experimental data at long wavelengths does not allow an effective constraints of estimated profiles at greater depths. Thus, the  $V_S$  oscillates between 330 m/s and 400 m/s, whereas  $D_S$  spans over a much broader range, mostly between 0.5% and 5% (that is, the variation is about one order of magnitude). This is the combined effect of the large variability in low-frequency attenuation data, the relevant influence of  $V_S$  on phase velocity and attenuation data, and the moderately low sensitivity of theoretical attenuation curves to  $D_S$  at great depths (e.g., Verachtert, 2018), that does not allow a constraint on  $D_S$  as effective as in the stiffness modeling. On the other hand, it should be noted that, particularly in the near-surface layers, both the velocity and dissipation structures show well defined trends.

In summary, the DAS technology can be successfully used to jointly estimate the phase dispersion and attenuation data, obtaining the same level of reliability of the canonical geophone array. Furthermore, the potentially stronger influence of incoherent noise on DAS data is balanced by the significant increase in the number of measurement points,

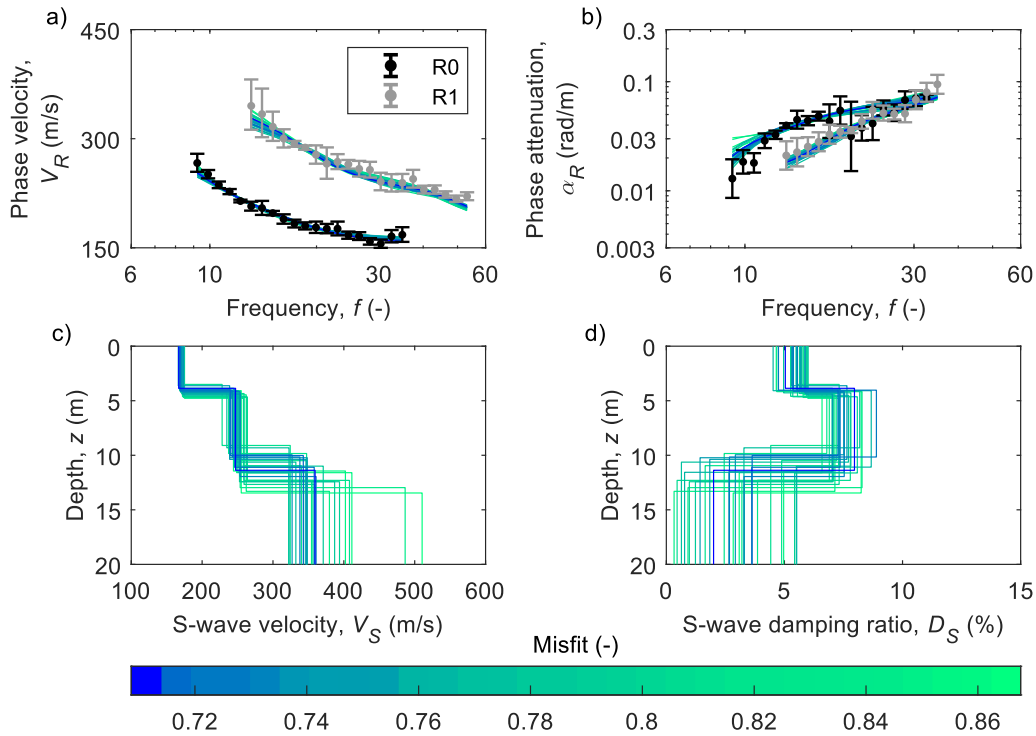


**Figure 5.** Best fitting inverted ground models to DAS experimental data from the Hornsby Bend site: a-b) Theoretical and experimental data for the phase velocity (a) and phase attenuation (b); c-d) Resulting S-wave velocity (c) and damping ratio (d) profiles; after Aimar et al. (2023).

thus resulting in a reduction in data variability, entailing an improvement in the accuracy of this system.

### 3.1.2 2D MASW using DAS

Two-dimensional (2D) MASW (e.g., Park, 2005) is a technique used to produce a pseudo-2D  $V_S$  cross-section of the subsurface by expanding upon the 1D MASW approach. This technique relies on spatially interpolating numerous 1D MASW  $V_S$  profiles obtained from overlapping sub-arrays along a linear testing alignment. One of the main challenges when performing 2D MASW using conventional equipment, such as geophones and 24-channel seismographs, is that the geophone spacing, the length of the sub-arrays, the spatial interval between sub-arrays, and the positions of shots relative to the sub-arrays must be determined prior to/during data acquisition, making it difficult to adjust them during data processing (i.e., after data acquisition). This poses a challenge because the geophone spacing and sub-array length can have a significant impact on the lateral resolution, maximum characterization depth, and anomaly detection capabilities (Yust et al., 2022). Therefore, the ability to modify parameters such as the sub-array length after initial processing results have been investigated can be highly advantageous. According to a study by Yust et al. (2022), the use of DAS rather than traditional 2D MASW

equipment can be highly advantageous in addressing these challenges.

In their recent study, Yust et al. (2022) investigated the effects of 2D MASW sub-array length using the DAS data collected at the Hornsby-Bend site. Three sets of sub-arrays with varying lengths were used to develop pseudo-2D  $V_S$  cross-sections along a 200 m long DAS line (refer to Figure 2a). The sub-arrays investigated by Yust et al. (2022) consisted of: (a) 12-channel sub-arrays approximately 11 m long, (b) 24-channel sub-arrays approximately 23 m long, and (c) 48-channel sub-arrays approximately 47 m long. They used an equivalent sub-array spatial interval of four channels (approximately 4 m) for all sub-arrays and performed 129 individual MASW analyses in total. The pseudo-2D  $V_S$  cross-sections obtained using the 12-, 24-, and 48-channel sub-arrays had lateral extents of 187.68 m, 175.44 m, and 150.96 m, respectively, while maintaining a consistent depth of 15 m, as shown in Figure 6a, 6b, and 6c, respectively. These cross-sections are quite similar over the top 7-8 m, but show noticeable differences at greater depths, highlighting the sensitivity of 2D MASW results to the choice of sub-array length. Nonetheless, each cross-section obtained from the different sub-array lengths was found to correlate better with a different key feature of the subsurface, as verified by comparisons with invasive data collected along the array alignment. For instance, Yust et al. (2022) found that, for the

Hornsby-Bend site, the most prominent impedance contrast in the  $V_s$  cross-section obtained using 12-channel sub-arrays corresponded to the depth of CPT refusal (see Figure 6a), while the  $V_s$  cross-section obtained using longer, 48-channel sub-arrays corresponded to the deeper shale impedance contrast, as indicated by the boring lithology log superimposed on the  $V_s$  cross-section (see Figure 6c). It is worth noting that Yust et al. (2022) were able to investigate these different sub-array lengths post data acquisition, owing to the flexibility allowed by DAS technology. Unlike traditional seismic equipment, DAS records the wavefield generated at each of the considered shot locations simultaneously along the entire length of the array at a constant channel separation, eliminating the need to pre-determine sub-array length and spatial sampling interval during data acquisition. This feature enables the investigation of multiple sub-array geometries during the processing stage of the analysis, thereby providing greater flexibility and control over acquisition parameters.

The study by Yust et al. (2022) shed light on the advantages of utilizing DAS in 2D MASW, and emphasized the significance of incorporating a priori information, such as invasive testing data, to fine-tune the 2D MASW analysis and achieve project-specific objectives, whenever feasible. In cases where there is insufficient conclusive information to constrain subsurface layering, Yust et al.

(2022) recommended examining multiple 2D MASW sub-array configurations to gain a comprehensive understanding of the subsurface conditions and accurately assess the uncertainty of the results.

### 3.1.3 Machine learning

In recent years, there has been a growing interest in utilizing deep learning/machine learning/artificial intelligence (DL/ML/AI) techniques for non-invasive subsurface imaging (Adler et al., 2021). For example, with a fully trained and adaptable neural network it would theoretically be possible to swiftly generate subsurface images directly from wavefield measurements without the need to perform costly and complicated inversions. Furthermore, this type of imaging could be performed by an analyst without any significant understanding of machine learning. This would enable the reuse of fully trained neural networks to rapidly produce site-specific results, eliminating the need for specialized expertise, which is often required by conventional inversion methods. To train a neural network for subsurface imaging, a large dataset consisting of numerous input-output image pairs is required. The input can be a representation of the raw data acquired from the field, or some post-processed version

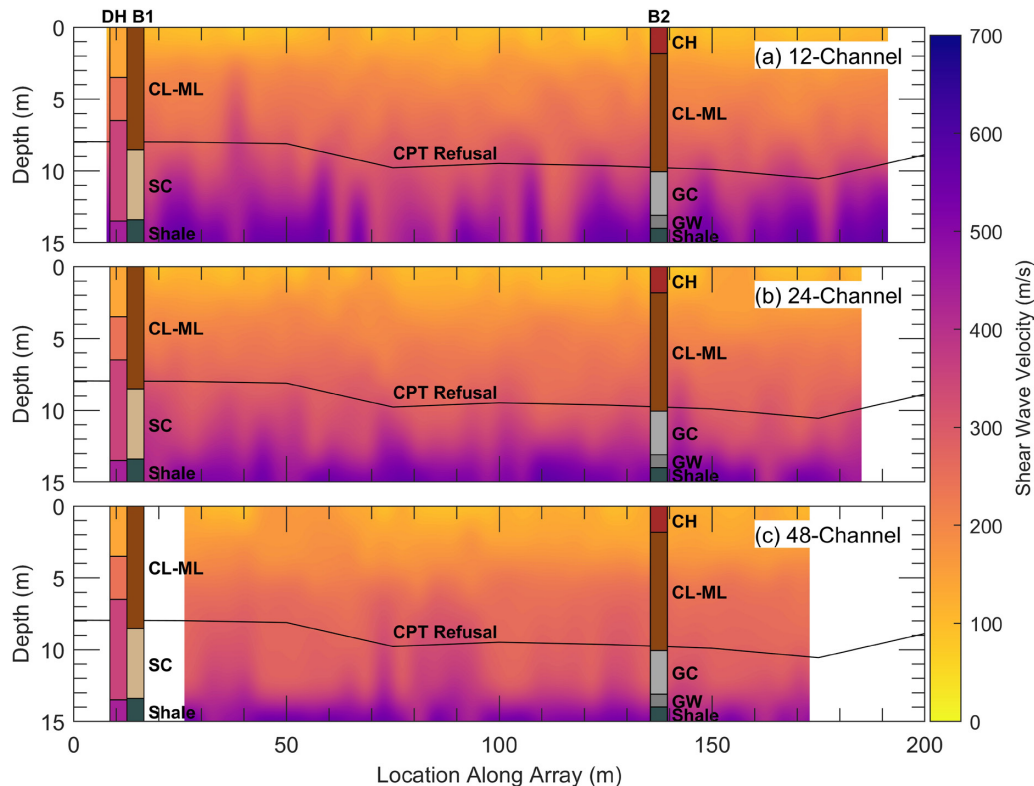


**Figure 6.** Pseudo-2D  $V_s$  cross-sections after Yust et al. (2022) from the: (a) 47, 12-channel MASW sub-arrays, (b) 44, 24-channel MASW sub-arrays, and (c) 38, 48-channel MASW sub-arrays inverted using a 15-layer inversion parameterization. The depths of refusal for 9 CPT soundings along the array are shown on all plots with a solid black line.

of it, while the output can be a subsurface image of the parameter of interest, such as a  $V_s$  cross-section. Due to the considerable number of image pairs needed to train a neural network, all research studies thus far have relied on numerically-developed image pairs, as in the case of the convolutional neural network (CNN) developed by Vantassel et al. (2022c), which takes a seismic wavefield input image and outputs a 2D  $V_s$  image. A significant challenge that has impeded the use of machine learning as an end-to-end imaging technique for real-field applications is the lack of generalizability (Li et al., 2020; Feng et al., 2022). In other words, these neural networks often struggle when presented with real-field data, particularly if the data was acquired using a different acquisition configuration than the one used during network training (e.g., Vantassel et al., 2022c).

Abbas et al. (2023b) have recently introduced a CNN that shows promise for rapidly generating 2D  $V_s$  images of near-surface soil-over-bedrock geology using real-field data. To train and test their CNN, they utilized 100,000 synthetic near-surface models with varying soil-over-bedrock conditions. Their CNN takes a frequency-dependent normalized dispersion image as input (rather than a seismic wavefield image) and produces a 2D  $V_s$  image as output, as illustrated schematically in Figure 7. Abbas et al. (2023b) demonstrated that while using different testing configurations in terms of source type, source offset, number of receivers, and receiver spacings leads to significantly different measured wavefields for the same subsurface structure, the normalized dispersion images processed from these different wavefields are quite similar, although not identical. Abbas et al. (2023b) leveraged this feature and demonstrated that a CNN trained on normalized dispersion images processed from wavefields acquired using a specific testing configuration can still perform well when presented with dispersion images processed from wavefields acquired using different testing configurations. This acquisition flexibility significantly improves the CNN's generalization capability, enabling it to be utilized as an end-to-end imaging method or as a tool to create rapid starting models for full-waveform inversion (FWI).

Abbas et al. (2023b) demonstrated the practical capability of their CNN by applying it to experimental field data collected at the Hornsby Bend site. Their CNN generated a high-resolution 48 m wide by 24 m deep  $V_s$  subsurface image, which agrees well with the actual subsurface structure determined through invasive tests conducted at the site, as shown in Figure 8, thereby establishing the CNN's promise in handling real-field data. While Abbas et al. (2023b) used geophone-derived dispersion images in their study, their approach is equally applicable to DAS-derived dispersion images, as geophone and DAS-derived dispersion images are shown to be equivalent by Vantassel et al. (2022b).

### 3.1.4 Full wave form inversion using DAS

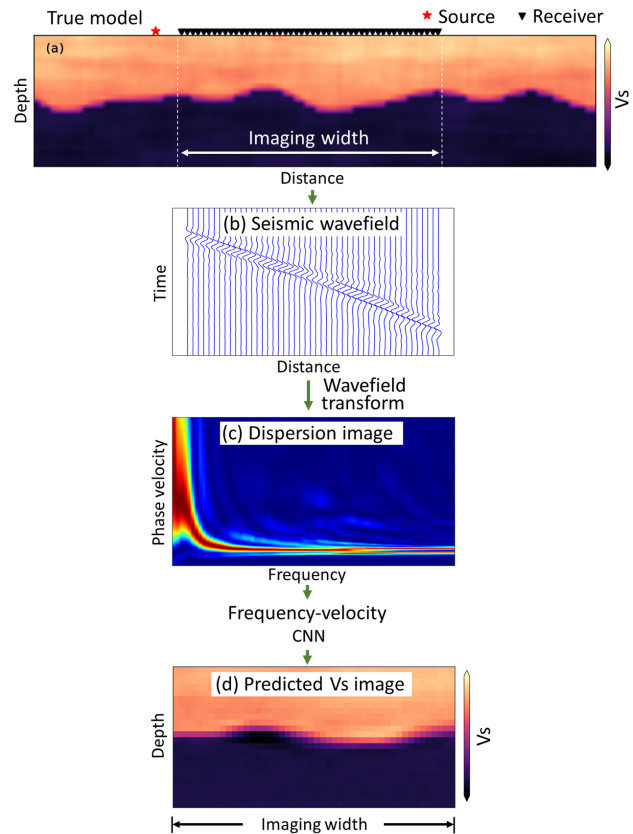


**Figure 7.** Illustrates the Frequency-velocity CNN framework introduced by Abbas et al. (2023b) for 2D  $V_s$  imaging of near-surface soil-over-bedrock geology. Panel (a) showcases a soil-over-rock 2D model featuring a 47-meter array of receivers and a single source located off the array's end. In panel (b), an example seismic wavefield recorded by the 48 receivers shown in panel (a) from a Ricker source is depicted. Panel (c) displays the associated dispersion image, serving as the input to the Frequency-velocity CNN. Finally, in panel (d), the Frequency-velocity CNN's predictions of the true synthetic 2D  $V_s$  images presented in panel (a) are showcased.

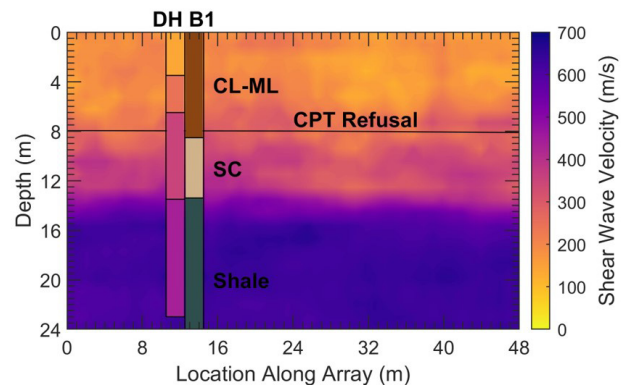


**Figure 8.** The frequency-velocity CNN output 2D  $V_s$  image for the Hornsby Bend site after Abbas et al. (2023b). For comparison with actual field conditions, a borehole log (i.e., B1) is superimposed on the predicted  $V_s$  image at 12.5 m, which is the location where the boring was conducted.

Full-waveform inversion (FWI) is a robust imaging technique that produces 2D/3D images of the subsurface by matching a synthetic seismic wavefield, generated by numerically solving the wave equation, to an experimental seismic wavefield acquired in the field. The process involves an iterative data-fitting procedure that requires modifying an initial model through which the synthetic waveforms propagate until the synthetic and experimental wavefields match, based on a selected inversion objective function. This is achieved by adjusting the material properties of the synthetic subsurface model, thereby reducing the misfit between the synthetic and recorded data. Unlike 2D MASW, which can only produce pseudo-2D images, FWI generates true 2D and 3D images by leveraging all available information in the seismic wavefield, including phase and amplitude. This sets FWI apart from other approaches, such as seismic refraction that relies only on wavefield first arrivals or surface wave testing that uses only Rayleigh dispersion. In addition to providing insights into material parameters like  $V_s$  and compression wave velocity ( $V_p$ ), which are of high interest to engineers, FWI can also be used to assess any other material properties that impact seismic wave propagation, such as density and damping ratio.

Despite its numerous advantages, FWI also encounters significant challenges. The computational costs associated with FWI are considerable, and the accuracy of its results can be heavily influenced by the initial model (Vantassel et al., 2022c; Yust et al., 2023), particularly in near-surface applications such as imaging the top 30 m. In the near surface, material properties tend to exhibit rapid variations over short distances, leading to a complex mixture of different wavefield components. This amalgamation includes compression, shear, and surface waves, which have not yet propagated far enough to separate from each other.

Traditionally, FWI analysis has utilized data acquired through geophones, which capture particle velocity wavefields. However, the high spatial resolution provided by DAS has garnered interest for use in FWI studies. Nonetheless, there is a dearth of literature on the use of FWI with DAS data for near-surface characterization, particularly in regards to directly inverting DAS strain data without first converting it to particle displacement or velocity.

In a recent study conducted by Yust et al. (2023), a direct inversion of strain measurements obtained from DAS was performed at the Hornsby Bend site. The study aimed to image a cross-section measuring 200 m wide and 30 m deep. Four distinct 1D and 2D starting models specifically tailored to the site were utilized. The first model was based on a 1D  $V_s$  profile obtained through traditional MASW testing. The second starting model utilized a 1D  $V_s$  profile derived from seismic down-hole invasive testing. The third starting model relied on the CNN 2D  $V_s$  subsurface model developed by Abbas et al. (2023b) and depicted in Figure 8. Lastly, the fourth model was constructed using the 2D MASW analysis with the 48-channel subarrays developed by Yust et al. (2022) and discussed in the 2D MASW section (refer to Figure 6). The four FWI starting models used by Yust et al. (2023) are visually depicted in Figure 9. Yust et al. (2023) inverted for  $V_s$ ,  $V_p$ , and density,  $\rho$ , while assuming constant quality factors to characterize the attenuation of compression and shear waves in the model. Nonetheless, they noted that the attenuation parameters significantly impact the FWI results and noted that additional studies are required to help constrain these values. Yust et al. (2023) observed enhancements in each of the initial models through the implementation of FWI. This improvement was evident when comparing the misfit between synthetic and recorded waveforms for both the initial and updated models. For example, Figure 10 illustrates the misfit between the synthetic and experimental waveforms of

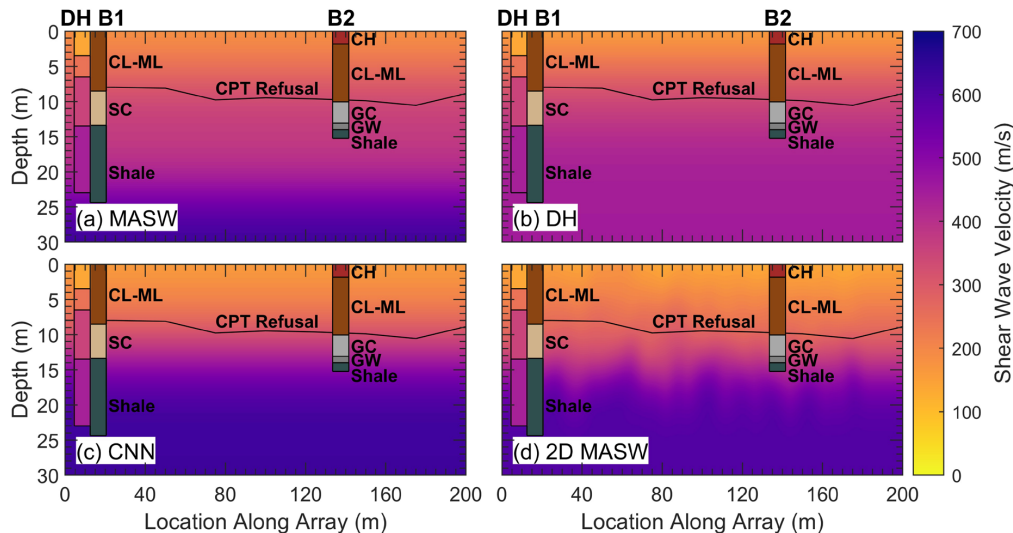


**Figure 9.** The four smoothed 2D  $V_s$  starting models used by Yust et al. (2023) for FWI based on: (a) 1D MASW, (b) downhole testing (DH), (c) CNN machine learning, and (d) pseudo-2D MASW.

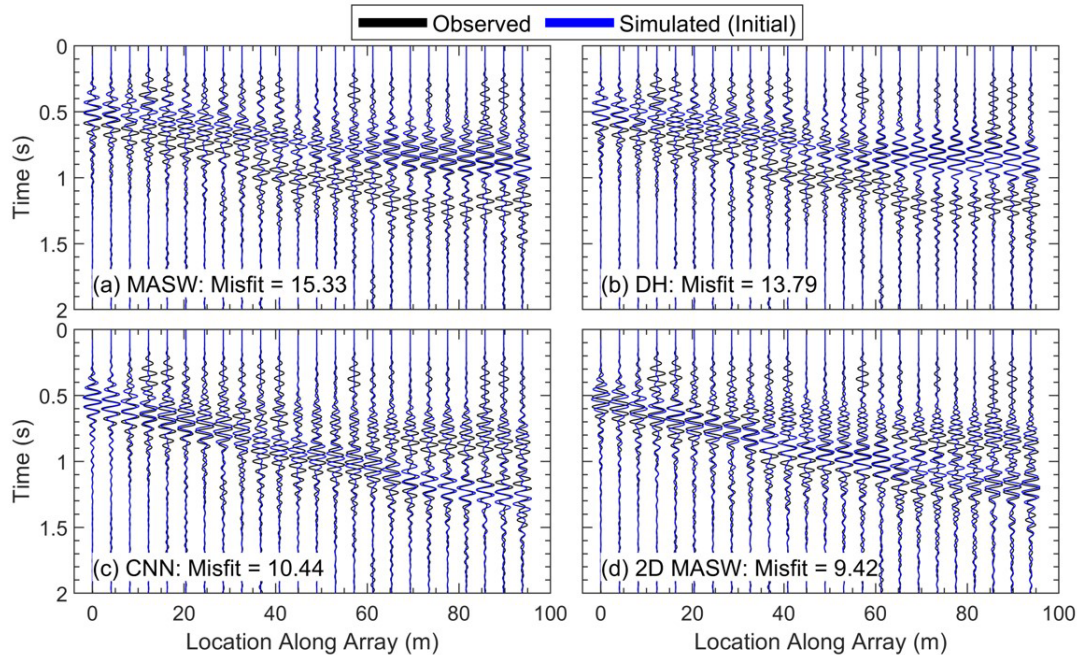


**Figure 10.** Normalized observed and simulated waveforms by Yust et al. (2023) from Shot 1 (–24 m) of Stage 1 (10 to 15 Hz) for the: (a) MASW, (b) downhole testing (DH), (c) CNN, and (d) 2D MASW starting models. GSOTD misfit values for each set of simulated waveforms are shown in the bottom left of each plot. Note that for clarity purposes, the waveforms are only shown for every fourth channel used for FWI.

the initial models, while Figure 11 displays the misfit for the FWI updated models following the first stage of a four-stage FWI. By comparing the waveform misfit values in Figure 10 and Figure 11, which are based on a graph space optimal transport distance (GSOTD) algorithm, one can clearly see that the FWI iterations in the first stage resulted in better waveform matches (i.e., lower misfit values) for all four starting models. This reduction in misfit values continued through each stage of the FWI process, ultimately resulting GSOTD misfit values for the four final models that were very similar to one another and only varied between 1.91 to 1.46. Despite the similarities in the final waveform misfit values, the final subsurface models did not vary significantly from their respective starting models and exhibited noticeable visual differences from one another, as depicted in Figure 12. Within the upper 7 m, the final  $V_s$  images are quite similar. Yet, below this depth there are evident disparities in the magnitudes and rates at which  $V_s$  increase. This finding highlights the intrinsic non-uniqueness associated with the FWI process, underscoring the importance of incorporating multiple starting models. Assessing the sensitivity of results to the choice of starting model and attaining consistent outcomes across different models engenders confidence in the subsurface regions where the models yield congruent results.

### 3.2 Discussion

In the preceding sections, various subsurface imaging techniques have been reviewed. This section aims to

provide an analysis of the advantages and disadvantages associated with each technique. The first method reviewed was 1D MASW, which is a well-established technique for  $V_s$  imaging using geophones. Extensive research supports this method, offering best practices and recommended workflows (Foti et al., 2018; Vantassel & Cox, 2022). However, this study presents two advancements to the conventional 1D MASW workflow. The first involves using DAS instead of geophones for data acquisition, while the second is the joint inversion for damping and  $V_s$ . The utilization of DAS significantly enhances measurement scales and spatial resolution beyond the capabilities of traditional measurement technologies. Moreover, when appropriate precautions are taken, the measurements obtained through DAS exhibit good agreement with those acquired using traditional methods like geophones (Daley et al., 2016; Hubbard et al., 2022; Vantassel et al., 2022b). It should be noted, though, that DAS provides deformation measurements only along the fiber optic cable direction, while geophones can capture particle motion point measurements in all three directions individually or simultaneously.

The second advancement focuses on the joint inversion for damping and  $V_s$  using data acquired through a 1D MASW setup, which represents a significant breakthrough, particularly due to the crucial role of damping in various domains, including site response. Aimar et al. (2023) showed that their approach is applicable on both geophone and DAS acquired data. Furthermore, this paper illustrates the innovative application

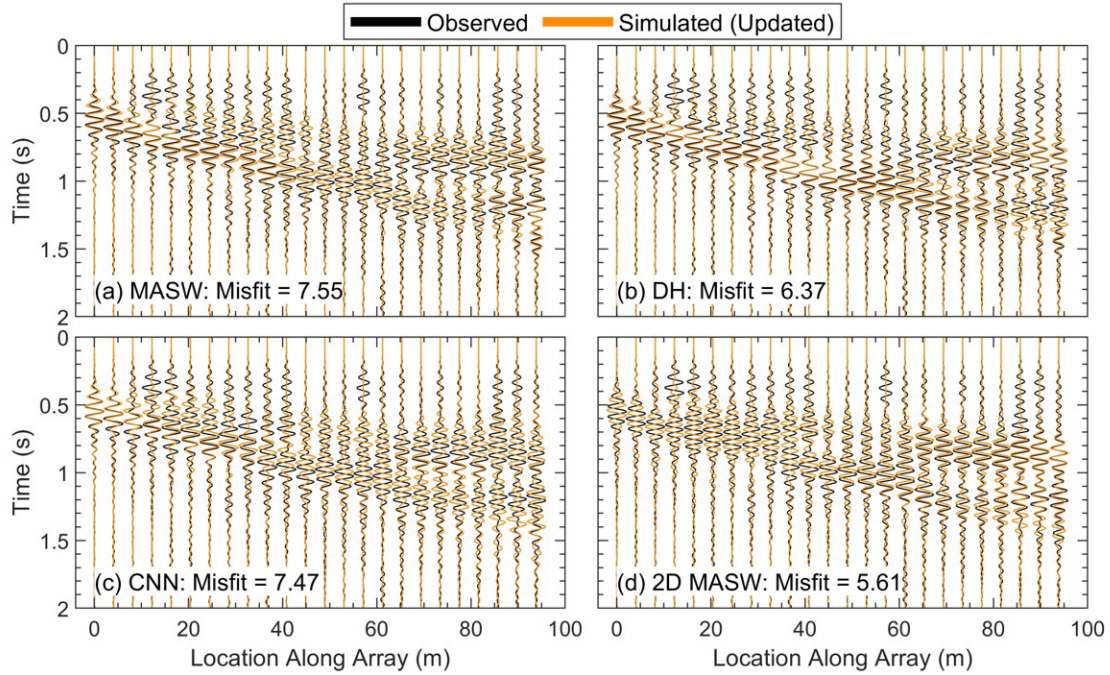


**Figure 11.** Normalized observed and simulated waveforms by Yust et al. (2023) from Shot 1 (–24 m) for the updated models at the end of FWI Stage 1 (10 to 15 Hz) based on the: (a) MASW, (b) downhole testing (DH), (c) CNN, and (d) 2D MASW starting models. GSOTD misfit values for each set of simulated waveforms are shown in the bottom left of each plot. Note that for clarity purposes, the waveforms are only shown for every fourth channel used for FWI.

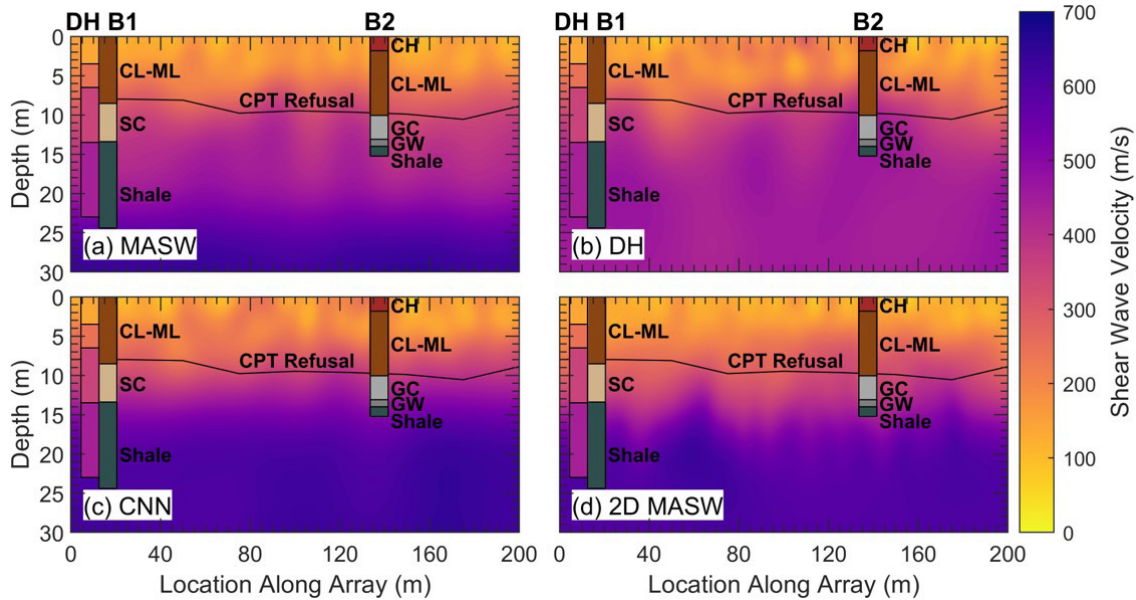


**Figure 12.** Borehole logs, downhole  $V_s$  results, and the depth to CPT refusal overlaid on the final, updated 2D  $V_s$  images at the end of FWI Stage 4 (10 to 30 Hz) for the: (a) MASW, (b) downhole testing (DH), (c) CNN, and (d) 2D MASW starting models after Yust et al. (2023).

of DAS in jointly characterizing the stiffness and dissipative parameters of a soil deposit based on a fiber-optic array. Figure 4 illustrates the favorable agreement between attenuation estimates obtained using both DAS and geophones for the Hornsby Bend site, with DAS-based measurements

exhibiting lower uncertainty compared to geophone-based measurements. However, the uncertainty in attenuation estimates generally tends to be higher than that observed for dispersion estimates, as detailed by Aimar (2022). In addition, the results presented were obtained from a portion

of a large experimental dataset. Future studies will thoroughly investigate these data to obtain a more comprehensive view of DAS performance compared to geophones and to seek for improved estimates of the phase attenuation, especially at low frequencies. It is worth noting that the 1D MASW technique generates a 1D subsurface profile by averaging the soil properties beneath the instrumentation array. To obtain a 2D representation of the subsurface, the 2D MASW technique was utilized. However, 2D MASW generates a pseudo 2D image rather than a true one, as it involves interpolating between multiple 1D MASW-derived soil profiles. Yust et al. (2022) demonstrated that this method produced  $V_s$  images that aligned with significant features at the Hornsby-bend site. Nevertheless, it was also observed that the resulting  $V_s$  image is reliant on the specific parameters chosen for data acquisition.

Another approach presented in this paper for 2D  $V_s$  imaging is the machine learning CNN proposed by Abbas et al. (2023b). This approach holds great promise as it can generate true 2D images of the subsurface, in contrast to the pseudo 2D images obtained through 2D MASW. Additionally, the machine learning approach is notable for its remarkable speed, as a trained neural network can deliver imaging results within seconds. However, this technique is still in its early stages of development and requires extensive research and testing before it can be reliably employed for subsurface imaging purposes.

The final imaging approach explored in this paper is 2D FWI. What sets FWI apart from the previously discussed methods is its utilization of the entire measured wavefield to generate true 2D and 3D subsurface images. Moreover, FWI differs from the machine learning approach by not operating as a black box method. As FWI continues to undergo further development, it is anticipated to become the preferred imaging technique. However, FWI currently faces several challenges, including notable computational costs and time-consuming complexity of the analysis process. Furthermore, studies by Yust et al. (2023) and Vantassel et al. (2022c) have demonstrated that the imaging results obtained through FWI are significantly influenced by the starting model used.

#### 4. Reference dataset: Newberry site, Florida

The preceding paragraphs have showcased the latest developments in seismic wave-based noninvasive subsurface imaging, with a practical demonstration of their potential at the Hornsby Bend site. However, it should be noted that the Hornsby Bend site is a relatively simple site with no documented underground anomalies. Furthermore, the seismic data from the Hornsby Bend site was collected using relatively short and linear DAS and geophone arrays. To provide researchers with a more comprehensive dataset at a more challenging site, Abbas et al. (2024) conducted a field test in Newberry, Florida, at a site known for its spatial variability, karstic voids, and underground

anomalies. The experiment utilized cutting-edge sensing technologies, including a two-kilometer DAS fiber optic cable, forming a dense 2D array of 1920 channels, and a 2D array of 144 SmartSolo three-component nodal stations to sense active-source and passive-wavefields, as illustrated schematically in Figure 13. The active-source data was generated using a powerful three-dimensional vibroseis shaker truck and impact sources, and it was simultaneously sensed by both the DAS and nodal stations. The vibroseis truck was used to vibrate the ground in the three directions (two horizontal and one vertical) at 260 locations inside and outside the instrumented array, while the impact sources were used at 268 locations within the array (refer to Figure 13). The passive wavefield data, recorded using the nodal stations, consisted of 48 hours of ambient noise collected over four days in four twelve-hour time blocks. The active-source and passive-wavefield DAS and nodal station data have been preprocessed and organized in an easy-to-navigate folder structure. The raw and processed data, along with detailed

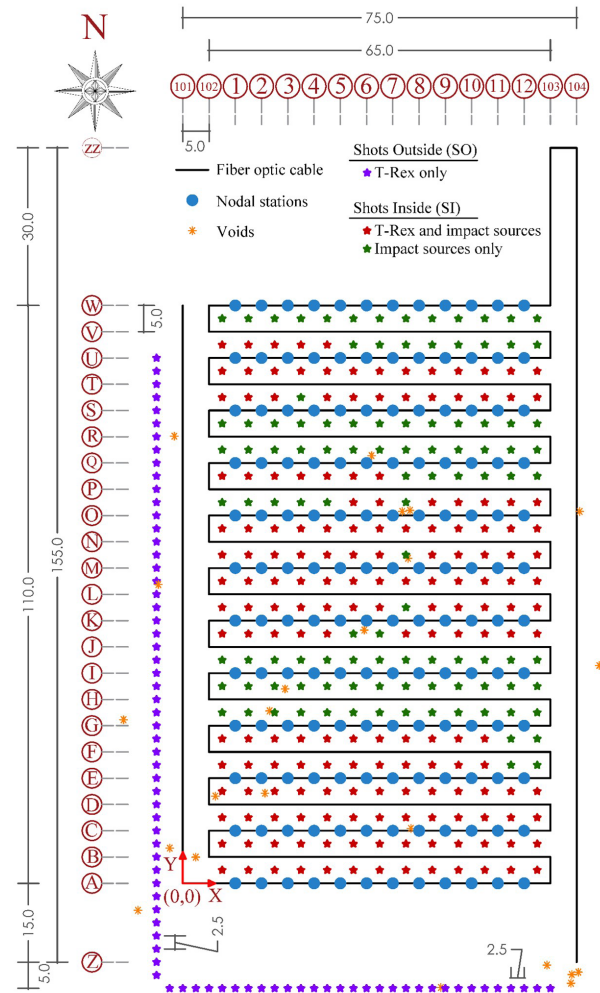


**Figure 13.** Newberry site testing configuration after Abbas et al. (2024).

documentation of the experiment and Python tools to aid in visualizing the DAS dataset have been archived and made publicly available on DesignSafe (Abbas et al., 2023a). The Newberry dataset (Abbas et al., 2024; Abbas et al., 2023a), featuring a powerful, triaxial vibroseis shaker and 3C sensors, in conjunction with the dense DAS array, offers a valuable resource for researchers exploring novel noninvasive subsurface imaging approaches that utilize seismic waves.

## 5. Conclusion

The paper covers advancements in noninvasive subsurface imaging technologies that utilize seismic waves for site characterization. These advancements span both innovative sensing technologies and advanced 1D and 2D imaging techniques for retrieving the small-strain shear modulus and damping ratio. Regarding sensing innovations, a particular focus is placed on the use of DAS as the data acquisition system for seismic wave sensing in near-surface imaging applications. In terms of imaging techniques, the joint inversion of attenuation and dispersion data is presented, utilizing 1D MASW in conjunction with either DAS or traditional sensing techniques such as geophones. With this approach, 1D shear wave velocity and damping profiles can be obtained. The presented 2D imaging techniques comprise 2D MASW using DAS, machine learning for 2D subsurface imaging, and 2D FWI using DAS data. All of these advancements, whether in sensing technologies or analysis methods, were implemented at the well-characterized Hornsby Bend site in Austin, Texas, enabling a discussion of the advantages and disadvantages associated with each method. Finally, a comprehensive and open-access subsurface imaging experiment conducted in Newberry, Florida, has been presented, where state-of-the-art technologies for sensing seismic waves and generating wavefields have been implemented.

## Declaration of interest

The authors have no conflicts of interest to declare. All co-authors have observed and affirmed the contents of the paper and there is no financial interest to report.

## Authors' contributions

Aser Abbas: conceptualization, writing – original draft, formal analysis, methodology, software. Mauro Aimar: conceptualization, writing – original draft, formal analysis, methodology, software. Michael Yust: visualization, formal analysis, software. Brady R. Cox: conceptualization, funding acquisition, project administration, writing – review & editing, supervision. Sebastiano Foti: conceptualization, funding acquisition, project administration, writing – review & editing, supervision.

## Data availability

Experimental datasets are available from the authors upon request.

## List of symbols and abbreviations

$2g$	gauge length
$e$	average strain, computed over the gauge length along the fiber-optic cable direction
$r$	spatial coordinate
$t$	time
$u$	ground displacement
$D_S$	shear wave damping ratio
$V_P$	compressional wave velocity
$V_R$	Rayleigh wave phase velocity
$V_S$	shear wave velocity
$\alpha_R$	Rayleigh wave phase attenuation
$\lambda$	wavelength
$\rho$	density (mass per unit volume)

## References

- Abbas, A., Cox, B.R., Tran, K.T., Corey, I., & Dawadi, N. (2024). An open-access data set of active-source and passive-wavefield DAS and nodal seismometer measurements at the Newberry Florida site. *Seismological Research Letters*, 1-17. Ahead of print. <http://dx.doi.org/10.1785/0220230216>.
- Abbas, A., Cox, B.R., Tran, K.T., Corey, I., Dawadi, N., & Menq, F.-Y. (2023a). *Active-source and passive-wavefield DAS and nodal station measurements at the Newberry Florida site*. DesignSafe-CI. <https://doi.org/10.17603/ds2-50eh-7v93>.
- Abbas, A., Vantassel, J.P., Cox, B.R., Kumar, K., & Crocker, J.A. (2023b). A frequency-velocity CNN for developing near-surface 2D vs images from linear-array, active-source wavefield measurements. *Computers and Geotechnics*, 156, 105305. <http://dx.doi.org/10.1016/j.comgeo.2023.105305>.
- Adler, A., Araya-Polo, M., & Poggio, T. (2021). Deep learning for seismic inverse problems: towards the acceleration of geophysical analysis workflows. *IEEE Signal Processing Magazine*, 38(2), 89-119.
- Aimar, M., Cox, B.R., & Foti, S. (July 5-7, 2023). Surface wave testing with distributed acoustic sensing measurements to estimate the shear-wave velocity and the small-strain damping ratio. In *Paper presented at the National Conference of Researchers in Geotechnical Engineering (CNRIG)*, Palermo, Italy.
- Aimar, M., Foti, S., & Cox, B.R. (2024a). Novel techniques for in-situ estimation of shear-wave velocity and damping ratio through MASW testing. Part I: a beamforming procedure

- for extracting Rayleigh-wave phase velocity and phase attenuation. *Geophysical Journal International*. In press.
- Aimar, M., Foti, S., & Cox, B.R. (2024b). Novel techniques for in-situ estimation of shear-wave velocity and damping ratio through MASW testing. Part II: a Monte Carlo algorithm for the joint inversion of phase velocity and attenuation. *Geophysical Journal International*. In press.
- Ajo-Franklin, J., Dou, S., Daley, T., Freifeld, B., Robertson, M., Ulrich, C., Wood, T., Eckblaw, I., Lindsey, N., Martin, E., & Wagner, A. (September 24-29, 2017). Time-lapse surface wave monitoring of permafrost thaw using distributed acoustic sensing and a permanent automated seismic source. In *Paper presented at the SEG Technical Program Expanded Abstracts 2017*, Houston, USA.
- Bakku, S.K. (2015). *Fracture characterization from seismic measurements in a borehole* [PhD thesis]. Massachusetts Institute of Technology.
- Bakulin, A., Silvestrov, I., & Pevzner, R. (2020). Surface seismics with DAS: an emerging alternative to modern point-sensor acquisition. *The Leading Edge*, 39(11), 808-818.
- Ciancimino, A., Lanzo, G., Alleanza, G.A., Amoroso, S., Bardotti, R., Biondi, G., Cascone, E., Castelli, F., Di Giulio, A., d'Onofrio, A., Foti, S., Lentini, V., Madiati, C., & Vessia, G. (2020). Dynamic characterization of fine-grained soils in Central Italy by laboratory testing. *Bulletin of Earthquake Engineering*, 18, 5503-5531.
- Comina, C., Foti, S., Boiero, D., & Socco, L.V. (2011). Reliability of VS<sub>30</sub> evaluation from surface-wave tests. *Journal of Geotechnical and Geoenvironmental Engineering*, 137(6), 579-586. [http://dx.doi.org/10.1061/\(ASCE\)GT.1943-5606.0000452](http://dx.doi.org/10.1061/(ASCE)GT.1943-5606.0000452).
- Connolly, D.P., Kouroussis, G., Laghrouche, O., Ho, C.L., & Forde, M.C. (2015). Benchmarking railway vibrations – track, vehicle, ground and building effects. *Construction & Building Materials*, 92, 64-81. <http://dx.doi.org/10.1016/j.conbuildmat.2014.07.042>.
- Costley, D.R., Galan-Comas, G., Kirkendall, C.K., Simms, J.E., Hathaway, K.K., Parker, M.W., Ketcham, S., Smith, E., Folks, W., Milburn, T., & Wadman, H.M. (2018). Spectral analysis of surface waves with simultaneous fiber optic distributed acoustic sensing and vertical geophones. *Journal of Environmental & Engineering Geophysics*, 23(2), 183-195.
- Cox, B., Wills, P., Kiyashchenko, D., Mestayer, J., Lopez, J., Bourne, S., Lupton, R., Solano, G., Henderson, N., Hill, D., & Roy, J. (2012). Distributed acoustic sensing for geophysical measurement, monitoring and verification. *CSEG Recorder*, 37(2), 7-13.
- Cox, B.R., & Wood, C.M. (2011). Surface wave benchmarking exercise: methodologies, results, and uncertainties. In C.H. Juang, K.K. Phoon, A.J. Puppala, R.A. Green & G.A. Fenton (Eds.), *Geo-Risk 2011: risk assessment and management* (pp. 845-852). American Society of Civil Engineers.
- Daley, T.M., Miller, D.E., Dodds, K., Cook, P., & Freifeld, B.M. (2016). Field testing of modular borehole monitoring with simultaneous distributed acoustic sensing and geophone vertical seismic profiles at Citronelle, Alabama. *Geophysical Prospecting*, 64(5), 1318-1334.
- Darendeli, M.B. (2001). *Development of a new family of normalized modulus reduction and material damping curves* [Doctoral thesis]. The University of Texas at Austin.
- Feng, S., Lin, Y., & Wohlberg, B. (2022). Multiscale data-driven seismic full-waveform inversion with field data study. *IEEE Transactions on Geoscience and Remote Sensing*, 60, 1-14.
- Fernandes, F.C., Moura, B.L.R., Almeida, M.S.S., Souza Junior, L.O., Tarazona, S.F.M., Almeida, M.C.F., & Barros, J.M.C. (2023). Determination of the dynamic parameters of Speswhite kaolin with resonant column and centrifuge tests. *Soils and Rocks*, 46(2), e2023013422. <http://dx.doi.org/10.28927/SR.2023.013422>.
- Foti, S. (2000). *Multistation methods for geotechnical characterization using surface waves* [PhD thesis]. Politecnico di Torino.
- Foti, S., Aimar, M., & Ciancimino, A. (2021). Uncertainties in small-strain damping ratio evaluation and their influence on seismic ground response analyses. In T.G. Sitharam, R. Jakka & S. Kolathayar (Eds.), *Latest developments in geotechnical earthquake engineering and soil dynamics* (pp. 175-213). Springer.
- Foti, S., Hollender, F., Garofalo, F., Albarello, D., Asten, M., Bard, P.-Y., Comina, C., Cornou, C., Cox, B., Di Giulio, G., Forbriger, T., Hayashi, K., Lunedei, E., Martin, A., Mercerat, D., Ohrnberger, M., Poggi, V., Renalier, F., Sicilia, D., & Socco, V. (2018). Guidelines for the good practice of surface wave analysis: a product of the InterPACIFIC project. *Bulletin of Earthquake Engineering*, 16(6), 2367-2420.
- Freifeld, B.M., Pevzner, R., Dou, S., Correa, J., Daley, T.M., Robertson, M., Tertyshnikov, K., Wood, T., Ajo-Franklin, J., Urosevic, M., & Gurevich, B. (May/June 30-2, 2016). The CO2CRC Otway Project deployment of a distributed acoustic sensing network coupled with permanent rotary sources. In *Paper presented at the 78th EAGE Conference and Exhibition 2016*, Vienna, Austria.
- Gabriels, P., Snieder, R., & Nolet, G. (1987). In situ measurements of shear-wave velocity in sediments with higher-mode Rayleigh waves. *Geophysical Prospecting*, 35(2), 187-196.
- Galan-Comas, G. (2015). *Multichannel analysis of surface waves using distributed fiber optic sensors* [PhD thesis]. Mississippi State University.
- Grattan, K.T.V., & Sun, T. (2000). Fiber optic sensor technology: an overview. *Sensors and Actuators A: Physical*, 82(1-3), 40-61.
- Hornman, K., Kuvshinov, B., Zwartjes, P., & Franzen, A. (June 10-13, 2013). Field trial of a broadside-sensitive distributed acoustic sensing cable for surface seismic.

- In European Association of Geoscientists & Engineers (Org.), *75th EAGE Conference & Exhibition incorporating SPE EUROPEC 2013* (pp. 1-5). London, UK: European Association of Geoscientists & Engineers. <https://doi.org/10.3997/2214-4609.20130383>.
- Hubbard, P.G., Vantassel, J.P., Cox, B.R., Rector, J.W., Yust, M.B.S., & Soga, K. (2022). Quantifying the surface strain field induced by active sources with distributed acoustic sensing: theory and practice. *Sensors*, *22*(12), 4589.
- Jousset, P., Reinsch, T., Ryberg, T., Blanck, H., Clarke, A., Aghayev, R., Hersir, G.P., Hennings, J., Weber, M., & Krawczyk, C.M. (2018). Dynamic strain determination using fibre-optic cables allows imaging of seismological and structural features. *Nature Communications*, *9*(1), 1-11.
- Kouroussis, G., Verlinden, O., & Conti, C. (2011). Free field vibrations caused by high-speed lines: measurement and time domain simulation. *Soil Dynamics and Earthquake Engineering*, *31*(4), 692-707.
- Krylov, V.V. (1995). Generation of ground vibrations by superfast trains. *Applied Acoustics*, *44*, 149-164. [http://dx.doi.org/10.1016/0003-682X\(95\)91370-1](http://dx.doi.org/10.1016/0003-682X(95)91370-1).
- Kuvshinov, B.N. (2016). Interaction of helically wound fibre-optic cables with plane seismic waves. *Geophysical Prospecting*, *64*(3), 671-688. <http://dx.doi.org/10.1111/1365-2478.12303>.
- Lancelle, C. (2016). *Distributed acoustic sensing for imaging near-surface geology and monitoring traffic at Garner Valley, California* [PhD thesis]. University of Wisconsin-Madison.
- Li, S., Liu, B., Ren, Y., Chen, Y., Yang, S., Wang, Y., & Jiang, P. (2020). Deep learning inversion of seismic data. *IEEE Transactions on Geoscience and Remote Sensing*, *58*(3), 2135-2149.
- Lombaert, G., & Degrande, G. (2003). The experimental validation of a numerical model for the prediction of the vibrations in the free field produced by road traffic. *Journal of Sound and Vibration*, *262*(2), 309-331.
- Lombaert, G., Degrande, G., Kogut, J., & François, S. (2006). The experimental validation of a numerical model for the prediction of railway induced vibrations. *Journal of Sound and Vibration*, *297*(3-5), 512-535.
- Madshus, C., & Kaynia, A.M. (2000). High-speed railway lines on soft ground: dynamic behaviour at critical train speed. *Journal of Sound and Vibration*, *231*(3), 689-701.
- Madshus, C., Lacasse, S., Kaynia, A.M., & Harvik, L. (July 27-31, 2004). Geodynamic challenges in high-speed railway projects. In *Paper presented at the Geotechnical Engineering for Transportation Projects*, Los Angeles, USA.
- Martakis, P., Taeseri, D., Chatzi, E., & Laue, J. (2017). A centrifuge-based experimental verification of Soil-Structure Interaction effects. *Soil Dynamics and Earthquake Engineering*, *103*, 1-14.
- Mateeva, A., Lopez, J., Potters, H., Mestayer, J., Cox, B., Kiyashchenko, D., Wills, P., Grandi, S., Hornman, K., Kuvshinov, B., Berlang, W., Yang, Z., & Detomo, R. (2014). Distributed acoustic sensing for reservoir monitoring with vertical seismic profiling. *Geophysical Prospecting*, *62*, 679-692.
- McMechan, G.A., & Yedlin, M.J. (1981). Analysis of dispersive waves by wave field transformation. *Geophysics*, *46*(6), 869-874.
- Menq, F.-Y. (2003). *Dynamic properties of sandy and gravelly soils* [Doctoral thesis]. The University of Texas at Austin.
- Mestayer, J., Karam, S.G., Cox, B., Wills, P., Mateeva, A., Lopez, J., Hill, D., & Lewis, A. (June 4-7, 2012). Distributed acoustic sensing for geophysical monitoring. In *Paper presented at the 74th EAGE Conference and Exhibition incorporating EUROPEC 2012*, Copenhagen, Denmark.
- Nolet, G., & Panza, G.F. (1976). Array analysis of seismic surface waves: limits and possibilities. *Pure and Applied Geophysics*, *114*(5), 775-790.
- Papadopoulos, K., Kuo, K., Germonpré, M., Verachtert, R., Zhang, J., Maes, K., Lombaert, G., & Degrande, G. (September 16-20, 2019). Numerical prediction and experimental validation of railway induced vibration in a multi-storey office building. In G. Degrande, G. Lombaert, D. Anderson, P. de Vos, P.-E. Gautier, M. Iida, J.T. Nelson, J.C.O. Nielsen, D.J. Thompson, T. Tielkes & D.A. Towers (Eds.), *Noise and vibration mitigation for rail transportation systems: proceedings of the 13th International Workshop on Railway Noise* (pp. 529-537). Cham, Switzerland: Springer.
- Park, C.B. (2005). *MASW - horizontal resolution in 2D shear-velocity (Vs) mapping*. Kansas Geological Survey.
- Park, C.B., Miller, R.D., & Xia, J. (1999). Multichannel analysis of surface waves. *Geophysics*, *64*(3), 800-808.
- Passeri, F. (2019). *Development of advanced geostatistical models of shear wave velocity profiles to manage uncertainties and variabilities in Ground Response Analyses* [PhD thesis]. Politecnico di Torino.
- Pyl, L. (2004). *Development and experimental validation of a numerical model for traffic induced vibrations in buildings* [Doctoral thesis]. KU Leuven.
- Robertson, P.K. (2009). Interpretation of cone penetration tests - a unified approach. *Canadian Geotechnical Journal*, *46*(11), 1337-1355.
- Rodriguez-Marek, A., Bommer, J.J., Youngs, R.R., Crespo, M.J., Stafford, P.J., & Bahrampouri, M. (2021). Capturing epistemic uncertainty in site response. *Earthquake Spectra*, *37*(4), 921-936.
- Santos, N.C., Colaço, A., Costa, P.A., & Calçada, R. (2016). Experimental analysis of track-ground vibrations on a stretch of the Portuguese railway network. *Soil Dynamics and Earthquake Engineering*, *90*, 358-380.
- Schevenels, M. (2007). *The impact of uncertain dynamic soil characteristics on the prediction of ground vibrations* [Doctoral thesis]. KU Leuven.
- Schevenels, M., Degrande, G., & François, S. (2009). *EDT: an elastodynamics toolbox for MATLAB*. Retrieved in December 20, 2023, from <https://bwk.kuleuven.be/bwm/edt>
- Soga, K., & Luo, L. (2018). Distributed fiber optics sensors for civil engineering infrastructure sensing. *Journal of*

- Structural Integrity and Maintenance*, 3, 1-21. <http://dx.doi.org/10.1080/24705314.2018.1426138>.
- Song, Z., Zeng, X., Thurber, C.H., Wang, H.F., & Fratta, D. (2018). Imaging shallow structure with active-source surface wave signal recorded by distributed acoustic sensing arrays. *Earthquake Science*, 31(4), 208-214. <http://dx.doi.org/10.29382/eqs-2018-0208-4>.
- Stewart, J.P., Afshari, K., & Hashash, Y.M.A. (2014). *Guidelines for performing hazard-consistent one-dimensional ground response analysis for ground motion prediction*. Pacific Earthquake Engineering Research Center. PEER Report 2014.
- Stokoe II, K.H., Cox, B.R., Clayton, P.M., & Menq, F. (2020). NHERI@UTexas experimental facility with large-scale mobile shakers for field studies. *Frontiers in Built Environment*, 6, 575973.
- Stokoe, K.H., & Santamarina, J.C. (November 19-24, 2000). Seismic-wave-based testing in geotechnical engineering. In *Paper presented at the ISRM International Symposium*, Melbourne, Australia.
- Tao, Y., & Rathje, E. (2019). Insights into modeling small-strain site response derived from downhole array data. *Journal of Geotechnical and Geoenvironmental Engineering*, 145, 04019023.
- Thompson, D. (2009). *Railway noise and vibration: mechanisms, modelling and means of control*. Elsevier.
- Timoshenko, S. (1927). Methods of analysis of statical and dynamical stresses in rail. In *Paper presented at the Second International Congress on Applied Mechanics*, Zurich, Switzerland.
- Vantassel, J., Cox, B., Hubbard, P., Yust, M., & Menq, F. (2022a). *Active-source, near-surface, surface-wave measurements using Distributed Acoustic Sensing (DAS) and traditional geophones, in Characterization of the NHERI@UTexas Hornsby Bend test site – v2*. DesignSafe-CI. <https://doi.org/10.17603/ds2-bz52-ep82>.
- Vantassel, J.P., & Cox, B.R. (2022). SWprocess: a workflow for developing robust estimates of surface wave dispersion uncertainty. *Journal of Seismology*, 26(4), 731-756. <http://dx.doi.org/10.1007/s10950-021-10035-y>.
- Vantassel, J.P., Cox, B.R., Hubbard, P.G., & Yust, M. (2022b). Extracting high-resolution, multi-mode surface wave dispersion data from distributed acoustic sensing measurements using the multichannel analysis of surface waves. *Journal of Applied Geophysics*, 205, 104776. <http://dx.doi.org/10.1016/j.jappgeo.2022.104776>.
- Vantassel, J.P., Kumar, K., & Cox, B.R. (2022c). Using convolutional neural networks to develop starting models for near-surface 2-D full waveform inversion. *Geophysical Journal International*, 231(1), 72-90. <http://dx.doi.org/10.1093/gji/ggac179>.
- Veletsos, A.S., & Meek, J.W. (1974). Dynamic behaviour of building-foundation systems. *Earthquake Engineering & Structural Dynamics*, 3(2), 121-138.
- Verachtert, R. (2018). *Deterministic and probabilistic determination of dynamic soil characteristics* [PhD thesis]. KU Leuven.
- Yavuz, S., Freifeld, B.M., Pevzner, R., Tertysnikov, K., Dzunic, A., Ziramov, S., Shulakova, V., Robertson, M., Daley, T.M., Kepic, A., Urosevic, M., & Gurevich, B. (May/June 30-2, 2016). Subsurface imaging using buried DAS and geophone arrays - preliminary results from CO2CRC Otway Project. In *Paper presented at the 78th EAGE Conference and Exhibition 2016*.
- Yu, C., Zhan, Z., Lindsey, N.J., Ajo-Franklin, J.B., & Robertson, M. (2019). The potential of DAS in teleseismic studies: insights from the Goldstone experiment. *Geophysical Research Letters*, 46(3), 1320-1328. <http://dx.doi.org/10.1029/2018GL081195>.
- Yust, M.B.S., Cox, B.R., Vantassel, J.P., & Hubbard, P.G. (2022). DAS for 2D MASW imaging: a case study on the benefits of flexible sub-array processing. *arXiv*, 2210.14261. Ahead of print.
- Yust, M.B.S., Cox, B.R., Vantassel, J.P., Hubbard, P.G., Boehm, C., & Krischer, L. (2023). Near-surface 2D imaging via FWI of DAS data: an examination of the impacts of FWI starting model. *Geosciences*, 13(3), 63. <http://dx.doi.org/10.3390/geosciences13030063>.